Research Square

Preprints are preliminary reports that have not undergone peer review.
They should not be considered conclusive, used to inform clinical practice,
or referenced by the media as validated information.

Thermodynamically driven typhoon wind hazard projections over the China seas and southeast coast under CMIP6 scenarios using a random forest full-track framework

Qing Wang

wang_q24@hdec.com

Zhejiang Huadong Mapping and Engineering Safety Technology Co., Ltd. https://orcid.org/0000-0002-1664-3399

Haojia Li

PowerChina Huadong Engineering Corporation Limited

Qiang Liu

Zhejiang Huadong Mapping and Engineering Safety Technology Co., Ltd.

Bote Wang

Zhejiang Huadong Smartlink Technology Co., Ltd.

Yushuai Liu

Zhejiang Huadong Mapping and Engineering Safety Technology Co., Ltd.

Xiaoming Zhan

Zhejiang Huadong Smartlink Technology Co., Ltd.

Mingfeng Huang

Zhejiang University

Research Article

Keywords:

Posted Date: November 24th, 2026

DOI: https://doi.org/10.21203/rs.3.rs-11478025/v1

License: This work is licensed under a Creative Commons Attribution 4.0 International License.
Read Full License

Thermodynamically driven typhoon wind hazard projections over the China seas and southeast coast under CMIP6 scenarios using a random forest full-track framework

Qing Wang[1,2], Haojia Li[2,3], Qiang Liu[1], Bote Wang[2], Yushuai Liu[1], Xiaoming Zhan[2], Mingfeng Huang[4]

[1] *Zhejiang Huadong Mapping and Engineering Safety Technology Co., Ltd., Hangzhou 310014, China*

[2] *Zhejiang Huadong Smartlink Technology Co., Ltd., Hangzhou, 311100, China*

[3] *POWERCHINA HUADONG ENGINEERING CORPORATION, Hangzhou*, 311100, *China*

[4] *Institute of Structural Engineering, Zhejiang University, Hangzhou, 310058, China*

Abstract: Typhoon wind hazards over the China seas threaten massive offshore wind fleets and coastal infrastructure, yet their response to climate change remains inadequately quantified for coastal and offshore engineering. This study investigates how thermodynamic climate forcing reshapes typhoon wind hazards over the China seas and southeast coast. Monthly mean sea surface temperatures from ten CMIP6 global climate models (1979–2100) drive a random forest-based tropical cyclone (TC) full-track simulation framework (RFFT). For the historical period (1979–2015) and the mid- (2019–2055) and late-21st century (2064–2100) under SSP245 and SSP585, 10,000-year synthetic TC ensembles are generated to derive 0.2°-resolution onshore and offshore extreme wind fields. Relative to the baseline, the fraction of western North Pacific TCs reaching typhoon intensity or above rises by 6.0 percentage points by mid-century and exceeds 60% by late century under SSP245. Projected extreme-wind changes show a pronounced positive latitudinal gradient. Under SSP585, wind speeds at an annual exceedance probability of 0.01 increase by up to 11% by mid-century and 15% by late century along the northern Jiangsu coast. Offshore extremes rise by up to 14%,

whereas changes south of Fujian lie within the inter-model spread. These projections provide spatially continuous design-wind modification factors for coastal hazard mitigation.

Keywords: Tropical cyclone; Climate change; CMIP6; Typhoon wind hazard; Extreme wind speed; Random forest full-track simulation

Abbreviations	Definition	Abbreviations	Definition
AEP	Annual Exceedance Probability	SSP	Shared Socioeconomic Pathway
CMA	China Meteorological Administration	SST	Sea Surface Temperature
CMIP6	Coupled Model Intercomparison Project Phase 6	TC	Tropical Cyclone
GCM	Global Climate Model	TD	Tropical Depression (Maximum wind speed <17.2 m/s)
IPCC	Intergovernmental Panel on Climate Change	TS	Tropical Storm (Maximum wind speed 17.2−24.4 m/s)
KDE	Kernel Density Estimation	STS	Severe Tropical Storm (Maximum wind speed 24.5−32.6 m/s)
LMI	Lifetime Maximum Intensity	TY	Typhoon (Maximum wind speed 32.7−41.4 m/s)
RCP	Representative Concentration Pathway	STY	Severe Typhoon (Maximum wind speed 41.5−50.9 m/s)
RF	Random Forest	SuperTY	Super Typhoon (Maximum wind speed ≥51.0 m/s)
RFFT	Random Forest-based Full-Track simulation framework	USGS	United States Geological Survey
MAE	Mean Absolute Error	WNP	Western North Pacific
IBL	Internal Boundary Layer	MRI	Mean Recurrence Interval
OOB	Out-of-bag	ENSO	El Niño–Southern Oscillation
CMA-STI	China Meteorological	RI	Rapid Intensification

1. Introduction

Global mean surface temperature has risen markedly since the 1950s, and the resulting climate change poses growing risks to coastal infrastructure. Tropical cyclones (TCs) concentrate that risk through their winds, rainfall and storm surge. Mei and Xie (2016) reported a 12–15% increase in typhoon intensity affecting East and Southeast Asia over the 37 years after 1977, together with a doubling to tripling of the proportion of Category 4–5 cyclones, which they linked to regional ocean warming. The lifetime maximum intensity (LMI), a key indicator of cyclone strength, has also migrated: Kossin et al. (2014) found a poleward shift of 53 km per decade in the Northern Hemisphere and 62 km per decade in the Southern Hemisphere between 1982 and 2012, and Wang and Toumi (2021) reported that LMI locations moved 30 km per decade closer to land as large-scale steering flows changed. Detection and attribution of these trends remain uncertain (Knutson et al., 2019; Wu et al., 2022). Physical understanding and high-resolution modelling nevertheless agree that TC precipitation (Knutson et al., 2020), intensity (Mei and Xie, 2016; Huang et al., 2022a) and the proportion of high-category storms (Arias et al., 2021) will increase with further warming. Projected changes in frequency and translation speed, by contrast, remain contested (Kossin, 2018; Moon et al., 2019; Lanzante, 2019). Quantifying how the confirmed intensification

translates into engineering quantities is therefore the starting point of this study.

These trends have direct consequences for coastal and offshore engineering. The China seas support the world's largest offshore wind market as well as offshore platforms, cross-sea bridges, and coastal defense systems, all of which are exposed to typhoon-force winds over water where long-term in-situ measurements are scarce. Typhoon wind fields are also the primary atmospheric forcing of storm-surge and wave models; any climate-driven change in the wind hazard therefore propagates into surge, wave, and structural-loading estimates. Quantifying the response of typhoon winds over the ocean to climate change is accordingly a prerequisite for climate-resilient design and operation of offshore and coastal infrastructure.

Current research on climate change impacts on TC activity primarily employs general circulation models (GCMs) and downscaling techniques, including dynamic and synthetic downscaling. Confidence in future climate projections is largely built upon the capability of climate models to reproduce observed historical climate variability. However, early GCMs' low resolution limited their capacity to model high-intensity storms (Davis, 2018), undermining confidence in predicting extreme precipitation and wind speed changes. Knutson et al (1998, 2004) employed a dynamic downscaling approach that uses GCM-derived environmental outputs as initial and boundary conditions for high-resolution regional models to better resolve TC structures. TC risk assessments require large sample sizes, around 10^4, but high-resolution numerical models are impractical for large-scale TC simulations. Instead, researchers use empirical, statistical, and statistical-dynamical models to conduct Monte Carlo simulations of TCs under warming climates. These models aim to assess wind hazard risks

effectively.

Synthetic downscaling generates large populations of synthetic TCs from reanalysis data or low-resolution GCM fields and is widely used for TC risk studies under climate change. The statistical–dynamical approach of Emanuel et al. (2006) seeds storms randomly, tracks them with large-scale steering flows and β-drift, and estimates intensity with the Coupled Hurricane Intensity Prediction System (Emanuel and Nolan, 2004). It has been applied to future TC frequency and intensity (Emanuel, 2013), precipitation (Emanuel, 2017), storm surge (Marsooli et al., 2019) and economic loss (Mendelsohn et al., 2012). For regional hazard assessment, Chen and Duan (2018) and Chen et al. (2021) built a statistical–dynamical track model and found fewer and weaker landfalling TCs over China under El Niño conditions. Xu et al. (2020) applied the statistical–deterministic framework of Emanuel et al. (2006) to five CMIP5 models and obtained widely divergent 50- and 100-year design wind speeds for East Asian cities (CCSM4, GFDL-CM3, HADGEM2-ES, MPI-ESM-MR and MRI-CGCM3), reflecting differing GCM interpretations of climate change.

TC intensity responds more directly to warming than track does. Intensity models for risk assessment are typically linear, nonlinear or hybrid regressions. The Vickery full-track framework (Vickery et al., 2000, 2009; Li and Hong, 2016; Huang et al., 2021), which underpins the hurricane wind hazard maps of ASCE/SEI 7-22 (Commentary C26.5), parameterises relative intensity through SST and tropospheric temperature (Darling, 1991) and can therefore simulate intensity under future climate variables. Mudd et al. (2014) applied it with SST fields for 2005 and 2100 and found that current design speeds are likely to be

exceeded more often in future. Chu et al. (2021) ran multi-millennial Vickery simulations with CCCma SSTs under RCP2.6, RCP4.5 and RCP8.5 and reported non-negligible effects on the wind speed distribution.

The Vickery method, however, partitions the ocean into 5°×5° (Vickery et al., 2000) or 2°×2° (Li and Hong, 2016) cells and fits regressions to the historical tracks and intensities in each cell, which often leaves too few samples for robust statistics. Cui and Caracoglia (2016) fitted the residuals with a Student's t distribution, and Cui et al. (2021) introduced QuadTree adaptive subdivision to refine the regression where data are dense. Assessing regression quality cell by cell remains laborious, and the absence of standard tuning rules limits the global applicability of the method, whose linear form also restricts its capacity to mine the data. Huang et al. (2022b) therefore developed a Random Forest full-track simulation method (RFFT) that trains track and intensity models on all TC data. It has been applied to extreme wind speeds at key cities along China's southeast coast (Huang et al., 2024).

Ten CMIP6 models provide the climate fields used to characterise sea-surface thermodynamic conditions in the WNP. Each GCM drives an independent simulation, and the resulting synthetic TCs are pooled across models to suppress individual-model bias. The period 1979–2015 serves as the historical baseline. Two Shared Socioeconomic Pathway scenarios are used for the future: SSP245, representing moderate social vulnerability and radiative forcing, and SSP585, in which radiative forcing reaches 8.5 W/m² by 2100. Both are analysed for the mid-21st century (2019–2055) and the late-21st century (2064–2100). The RF-based full-track method (RFFT) then yields extreme wind speeds for each climate state,

and the resulting anomalies show a pronounced latitudinal gradient consistent with the projected SST pattern.

Relative to existing climate-scale TC hazard studies, this work contributes in three aspects. It is, to the authors' knowledge, the first application of a machine-learning full-track TC simulator driven by a multi-model CMIP6 ensemble to quantify wind hazards over the China seas, enabling spatially continuous (0.2°) hazard mapping over both land and ocean rather than grid-by-grid regression. The experimental design deliberately isolates the thermodynamic component of climate change while holding kinematic parameters at their historical baseline, providing a controlled, attributable benchmark that complements fully coupled dynamic–thermodynamic projections (e.g., Chen et al., 2021). Finally, projections are reported as conditional design values associated with annual exceedance probabilities, with climate-model uncertainty explicitly separated from Monte Carlo sampling uncertainty, so that the results can be transferred into engineering practice as climate change modification factors.

2. Theoretical background

2.1 RF-based TC full track simulation method

The RF full-track model developed here builds on Huang et al. (2022b). Its advantage is that it avoids the spatial discretisation of traditional methods while preserving trajectory coherence, and that four cluster-specific movement models add spatial precision. The essential innovation is to dispense with cell-by-cell regression, such as the 5°×5° grids of Vickery et al. (2000), and to learn directly from continuous track data, which improves both

computational efficiency and physical consistency. The model is trained on the CMA best-track dataset (Ying et al., 2014; Lu et al., 2021), which documents landfalling TCs in China more reliably than the JMA or JTWC datasets (Yu et al., 2007). The CMA intensity classification is adopted throughout: tropical depression, tropical storm, severe tropical storm, typhoon, severe typhoon and super typhoon.

(a) Random forests

This study employs the Random Forest (RF) algorithm (Breiman, 2001) to develop the TC models. RF aggregates multiple Classification and Regression Trees (CARTs) trained on bootstrap samples; the samples left out of each bootstrap replicate (out-of-bag, OOB) provide an internal error estimate, and the OOB residuals are used to construct the stochastic perturbation terms of the Monte Carlo simulations. The OOB error depends mainly on the number of trees and the number of variables considered per split (Breiman, 2001), which are tuned to balance predictive accuracy against the computational cost of repeated TC simulations.

(b) TC generation models

When a TC full track simulation begins, TC genesis is statistically sampled following the historical statistics of TC occurrence. The annual occurrence number of historical TCs is counted from the CMA best-track dataset (Ying et al., 2014; Lu et al., 2021). A negative binomial distribution model (Vickery et al., 2000), used to fit the TCs' annual occurrence number, is expressed as follows:

153 $$p(x)=\binom{x+r-1}{x}(1-p)^{x}\,p^{r} \tag{1}$$

154 where r and p are the distribution parameters, which can be determined by curve fitting to the
155 historical data.

156 *(c) TC movement models*

157 Based on the four TC clusters classified by Huang et al. (2022b), we extract dynamic TC
158 location variables, specifically the latitude and longitude of the TC center, to train four
159 distinct RF-based movement models, with each model corresponding to one cluster. The
160 movement model is expressed as follows:

161 $$\begin{cases}\psi_{i+1}=RF_{\psi}(\psi_i,\lambda_i,\psi_{i-1},\lambda_{i-1},\psi_{i-2},\lambda_{i-2},\psi_{i-3},\lambda_{i-3})+\varepsilon_{\psi}\\ \lambda_{i+1}=RF_{\lambda}(\psi_i,\lambda_i,\psi_{i-1},\lambda_{i-1},\psi_{i-2},\lambda_{i-2},\psi_{i-3},\lambda_{i-3})+\varepsilon_{\lambda}\end{cases} \tag{2}$$

162 where RF_{ψ} and RF_{λ} denote the RF-based TC movement models to respectively predict the
163 latitude ψ (°) and longitude λ (°) for the next state (i+1) of a moving TC center; here, TC
164 locations from the four preceding time steps, i.e., i, i-1, i-2 and i-3, are selected as model input
165 variables. By fitting the residuals of the predicted OOB results to a normal distribution,
166 stochastic error terms ε_{ψ} and ε_{λ} are sampled from the fitted distribution and adopted as
167 perturbation terms for Monte Carlo simulations.

168 A deterministic termination condition, such as a prescribed low intensity (Jing and Lin,
169 2019) or central pressure difference (Cui et al., 2021), is often used in full track typhoon
170 simulations. TC termination can be modeled probabilistically using statistical distributions of
171 central pressure difference and lifecycle duration. In this study, a probabilistic termination
172 condition with the given termination probability is used for ending each simulated TC event.

Corresponding to four classified track clusters, four TC termination classifiers could be established:

$$end_{i+1} = RF_{end}\left(\psi_i, \lambda_i, p_{c,i}, T_{s,i}, N_i\right) \quad (3)$$

where RF_{end} is the TC termination classifier based on random forest algorithm; N_i (h) is the duration of storms from the beginning to the time step *i*; latitude ψ_i (°) and longitude λ_i (°) indicate the geographical location of the TC center; the central pressure $p_{c,i}$ (hPa) and sea surface temperature $T_{s,i}$ (K) are two variables to capture the current intensity condition. $T_{s,i}$ represents the monthly mean sea surface temperature interpolated to the specific geographical location of the TC center at time step *i*. The TC will keep on developing when $end_{i+1}=0$, and it comes to an end when $end_{i+1}=1$ (Huang et al., 2022b).

(d) TC Intensity model

The RF-based TC intensity model is developed for the entire WNP using all historical TC data. It adopts the same relative intensity definition as the original Vickery model to quantify storm strength:

$$I_{i+1} = RF_I\left(\psi_i, \lambda_i, I_i, I_{i-1}, I_{i-2}, T_{s,i+1}, T_{s,i}, T_{s,i-1}, T_{s,i-2}, p_{c,i}, p_{c,i-1}, p_{c,i-2}\right) + \varepsilon_I \quad (4)$$

The RF TC intensity model predicts the relative intensity at the next time step, denoted as RF_I. Key predictors include: latitude ψ_i (°), longitude λ_i (°), the relative intensity *I* defined by Darling (1991), the central pressure p_c (hPa) and the monthly mean sea surface temperature T_s (K). The relative intensity *I* converts the TC central pressure difference into a relative metric by incorporating environmental factors like SST and humidity. It is defined as $I = (p_{da} - p_c + e_s)/(p_{da} - p_{dc})$, where p_{da} (hPa) is the ambient environmental pressure, p_c (hPa) is the TC central pressure, and p_{dc} (hPa) is the minimum sustained dry pressure. The saturation vapor pressure e_s incorporates the thermal forcing, calculated as $e_s = 6.112 \times \exp[17.67 \times (T_s - 273)/(T_s - 29.5)]$. A random error term ε_I is incorporated. The

number of decision trees is set as 50 to build the TC intensity model.

Typically, a TC experiences a significant intensity decline after landfall due to the loss of oceanic energy and dissipation caused by rough terrain. A filling rate model for landfalling TCs, proposed by Vickery (2005), is expressed as follows:

$$\Delta p(t) = \Delta p_0 \exp(-\kappa t) \tag{5}$$

where Δp_0 (hPa) represents the central pressure difference at TC landfall; $\Delta p(t)$ (hPa) denotes the central pressure difference t hours post-landfall; $\kappa = \kappa_0 + \kappa_1 \Delta p_0 + \varepsilon_\kappa$, $\kappa > 0$; and empirical coefficients of κ_0, κ_1, along with the random error term ε_κ, are derived through regression analysis of historical landfalling TCs, as reported by Li and Hong (2016).

2.2 Coupled Model Intercomparison Project

The Coupled Model Intercomparison Project (CMIP), initiated in 1995 by the WCRP Working Group on Coupled Modelling (WGCM), provides standardized protocols and shared data for global coupled climate models, with its outputs underpinning successive IPCC assessment reports (Taylor et al., 2012). CMIP6 (Eyring et al., 2016) features the most advanced simulations and the most comprehensive experiment design to date.

Among the CMIP6-endorsed MIPs, the Scenario Model Intercomparison Project (ScenarioMIP; O'Neill et al., 2016) updates the CMIP5 RCP framework (RCP2.6, RCP4.5, RCP6.0, RCP8.5) by combining the Shared Socioeconomic Pathways (SSPs) with radiative forcing levels of 1.9–8.5 W/m² by 2100 (e.g., SSP1-2.6, SSP2-4.5, SSP3-7.0, SSP5-8.5).

The SSP framework comprises five pathways (SSP1 sustainability, SSP2 middle-of-the-road, SSP3 regional rivalry, SSP4 inequality, SSP5 fossil-fueled development), incorporating quantitative factors (e.g., GDP, population) and qualitative aspects (e.g.,

lifestyle, technology). This study examines SSP245 (a medium-emission stabilization pathway) and SSP585 (a high-emission pathway reaching 8.5 W/m² by 2100), which serve as standard benchmark scenarios in IPCC AR6 and effectively bound the probable range of future climate forcing (Hausfather and Peters, 2020).

Ten CMIP6 GCMs are used to analyse SST and the associated environmental variables in the WNP. The Historical experiment is driven by observed time-varying forcings, including greenhouse gases, through 2014 (Eyring et al., 2016), whereas SSP245 and SSP585 follow prescribed medium and high emission pathways from 2015 onward. Model details are given in Table 1. A ten-model ensemble is used to reduce epistemic uncertainty and to capture the spread of projected climate responses. All selected models provide continuous monthly mean SST for the Historical, SSP245 and SSP585 experiments, which ensures methodological consistency across the future simulations.

3. TC simulation under CMIP6 climate change scenarios

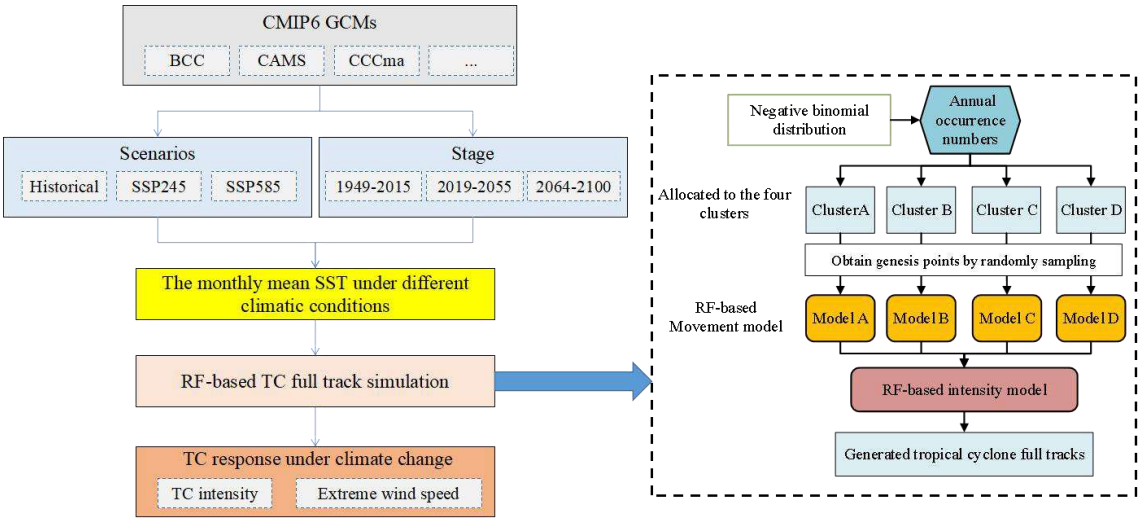


Fig. 1. The flow chart of TC wind hazards estimation under CMIP6 climate change scenarios by the RF-based TC full track simulation. The RF models are trained on the full CMA record (1949–2015), whereas the historical baseline used for validation and for the modification factors is 1979–2015.

Fig. 1 summarises the RFFT workflow. Environmental fields from the Historical period (1979–2015) and from the mid- (2019–2055) and late-21st century (2064–2100) under SSP245 and SSP585 drive the RF-based full-track simulator. Genesis points are sampled from a negative binomial distribution (Li and Hong, 2016; Huang et al., 2021) conditioned on historical tracks; four genesis types are drawn at random (Huang et al., 2022b) and four RF movement models predict subsequent positions. A unified RF intensity model and a filling-rate model (Vickery, 2005) then set intensity, followed by a termination check (Huang et al., 2022b). Repeating the procedure yields 1,000 years of tracks and intensities per GCM, pooled into a 10,000-year ensemble for each climate state (Section 3.3). The Meng wind-field model (Meng et al., 1995; Huang et al., 2021) then produces the three-dimensional wind fields from which extreme speeds and hazard levels are derived.

3.1 Analysis of sea surface temperature variability in the WNP

Annual mean SST over the WNP (95°E–180°E, 0°N–70°N) exhibits a robust warming trend from 1970 to 2100 in the ensemble of 10 CMIP6 GCMs (Fig. 2, Table 1). As the original CMIP6 models have coarse resolutions (Table 1), regridding to 0.1° using bilinear interpolation is required to match the spatial step of the RFFT model, ensuring smooth and physically consistent local thermodynamic inputs. The multi-model mean is shown by solid lines, while individual model simulations are represented by dashed lines. Three distinct phases are presented: 1) Historical simulations (blue curve, 1970–2014); 2) SSP245 scenario projections (yellow curve, 2015-2100); 3) SSP585 scenario projections (red curve, 2015-2100).

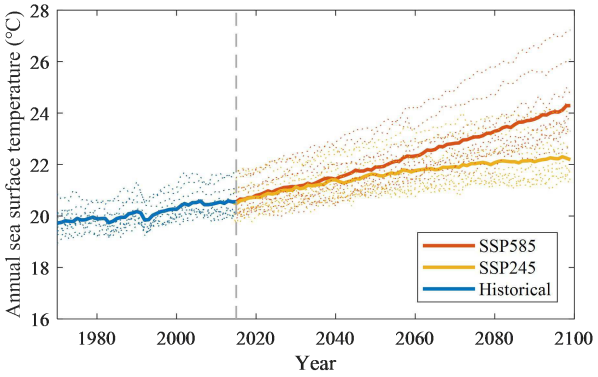


Fig. 2. Annual mean SST changes in the WNP (1970-2100).

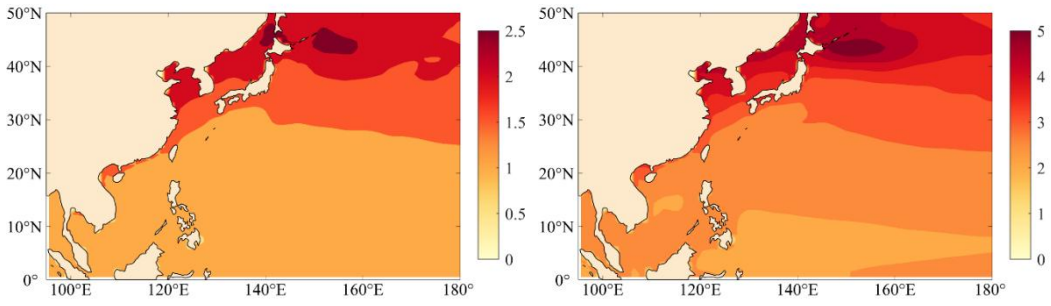
Table 1. Basic information on the ten GCMs of CMIP6.

Model Name	Issuing Agency	Country	Horizontal Grid Resolution (°)	Vertical Pressure Levels
BCC-CSM2-MR	BCC	China	1.13×1.13	19
CAMS-CSM1-0	CAMS	China	1.13×1.13	19
CanESM5	CCCma	Canada	2.81×2.81	19
CESM2-WACCM	NCAR	USA	1.25×0.90	19
FGOALS-f3-L	CAS	China	1.00×1.00	19
INM-CM5-0	INM	Russia	2.00×1.50	19
MIROC6	MIROC	Japan	1.41×1.41	19
MPI-ESM1-2-LR	MPI-M	Germany	1.88×1.88	19
MRI-ESM2-0	MRI	Japan	1.13×1.13	19
NorESM2-MM	NCC	Norway	1.25×0.90	19

The multi-model ensemble projects significant warming of annual mean SST in the WNP across all scenarios (Fig. 2). Under the Historical scenario, the regional SST increased by 0.9°C from 19.7°C in 1970 to 20.6°C in 2014 (a 4.6% rise). For the SSP245 scenario, the SST is projected to increase by 1.6°C from 20.6°C in 2014 to 22.2°C by 2100 (7.8%), with the

warming rate gradually slowing after the 2060s attributable to prescribed increases in forest area (approximately 331 million hectares) and controlled CO2 emissions (Hurtt et al., 2020). The most pronounced warming occurs under the SSP585 scenario, reaching 24.3°C by 2100, an increase of 3.7°C (18.0%) relative to 2014 levels.

Fig. 3 shows the projected monthly SST anomalies under SSP245 and SSP585, averaged over the ten CMIP6 GCMs. Typhoon-season (July–November) mean SST was computed for each model, smoothed with 20-year moving averages to remove interannual noise such as ENSO, and compared between 2000–2020 and 2080–2100. All outputs were regridded to 0.1°×0.1° by bilinear interpolation.



(a)SSP245 (b)SSP585

Fig. 3. CMIP6 multi-model ensemble projections of monthly SST anomalies in the WNP (2080–2100 relative to the 2000–2020 contemporary baseline). Note: The contemporary period (2000–2020) is used solely for illustrating the spatial distribution of SST anomalies and is independent of the historical dataset used for machine-learning model training.

The spatial distribution of typhoon-season SST anomalies (Fig. 3) reveals pronounced regional variability, with maximum warming exceeding 2.5°C (SSP245) and 5.0°C (SSP585) in high-latitude zones and East Asian coastal waters. Particularly, the amplified coastal warming may substantially increase the peak intensity of landfalling typhoons across China, Japan, Korea, and adjacent regions through elevated ocean heat content. The projected thermal expansion of favorable conditions for tropical cyclones into higher latitudes implies

prolonged maintenance of storm intensity during northward propagation, potentially exacerbating typhoon-related hazards in normally less-affected regions (Kossin et al., 2016).

3.2 Evolution of typhoon intensity under climate change

Building upon previous examination of spatiotemporal SST variations in the WNP under SSP245 and SSP585 scenarios—which suggested significant future intensification of typhoons near China's coast—this study employs the RF-based full track simulation framework to quantify potential changes in typhoon intensity and engineering extreme wind speeds.

The modeling system integrates thermal forcing conditions from CMIP6 GCM projections, utilizing Historical simulations (1979–2015) as the baseline and future projections for the mid- (2019–2055) and late-21st century (2064–2100) under both scenarios. The typhoon simulations are driven by monthly mean SST extracted from the CMIP6 models. This variable is coupled to determine the environmental thermodynamic capacity (e.g., saturation vapor pressure), governing TC intensity variations across different scenarios. While these thermodynamic conditions evolve under future climates, dynamic parameters (specifically TC genesis location, frequency, translation speed, and track distribution) remain stationary at historical baselines. This framework thus strictly isolates the thermodynamic-driven responses of TC extreme wind speeds.

A dual-period data strategy is used to limit modelling uncertainty and observational bias. The Random Forest models are trained on the full CMA record from 1949 to 2015, which maximises the sample and captures TC dynamic behaviour robustly. Baseline evaluation and

intensity validation are restricted to 1979–2015, the 37-year span bounded by the advent of comprehensive satellite remote sensing, which removed the large pre-satellite intensity biases (Ying et al., 2014), and by the end of the CMIP6 Historical experiments in December 2014. The single year 2015 is the branch-off year of the SSP simulations and is retained so that the baseline length matches that of the future windows; because all scenarios start from the same state in that year, its inclusion does not introduce a scenario-dependent baseline. Because 37 years exceeds the 30-year climatological normal recommended by the World Meteorological Organization, it is statistically sufficient to represent a stable multi-decadal climate state.

Only one time-varying thermodynamic field is taken from the CMIP6 models: monthly mean SST. The SST field driving each simulation is a delta-change construction: the observed year-to-year monthly SST of 1979–2015 is combined with the ten-model mean monthly SST change of the target window, so the climate signal enters as a monthly climatological anomaly while the observed interannual variability of the historical period is retained. A simulated TC therefore experiences, at each 6-h step, the monthly SST of its own calendar year and month interpolated at its own position; the change between consecutive steps within a single storm reflects mainly the spatial SST gradient along the track rather than a temporal trend. The remaining variables, ambient pressure (1010 hPa) and relative humidity (0.75), are prescribed as empirical constants throughout training and prediction, following the thermodynamic assumption of the Vickery framework (Vickery et al., 2000; Darling, 1991). Because RH is constant across climate states, it enters the relative intensity only as a fixed multiplier on the saturation vapour pressure e_s; that multiplier is absorbed by the empirical calibration and does

not affect the SST-driven response, so the definition in Section 2.1(d) is written in terms of e_s directly. This configuration keeps feature consistency within the machine-learning framework and isolates the thermodynamic intensity response to SST. The time-varying SST enters only the termination classifier (Eq. 3) and the intensity model (Eq. 4). Full formulations are given by Darling (1991) and Huang et al. (2022b).

(a) TC simulation in historical climate

About 50% of historical WNP TCs (1979–2015) reached typhoon intensity or above at their lifetime maximum intensity, and reproducing that distribution is a prerequisite for the risk assessment that follows. Projections based on CMIP models show wide inter-model variability arising from differences in resolution and in model bias; Chen et al. (2021), for example, obtained 100-year design speeds for Shanghai by 2100 ranging from a 3.7 m/s decrease (CCSM4) to a 7.4 m/s increase (GFDL-CM3), and adopted a multi-model mean. Accordingly, 1,000-year RFFT simulations driven by the Historical fields of the ten GCMs are first evaluated against observations (Figs. 4–6), a length that is statistically sufficient for the bulk intensity distribution. The LMI distribution of each GCM is compared with the CMA statistics to assess how well the observed category proportions are reproduced.

In Fig. 4 the blue boxes show the category proportions simulated by each of the ten GCMs and the red boxes those of the CMA-STI dataset and of the GCM ensemble, defined as the pooled sample generated independently by the ten GCMs (1,000 years per model, 10,000 years in total). The ensemble agrees with the CMA statistics substantially better than individual models, indicating that pooling mitigates individual-model bias. It still

underestimates tropical depressions by 8% (6% simulated against 14% observed), which probably reflects an inherent limitation of the RF intensity model, whose training data bias it toward higher intensities at the expense of weak systems.

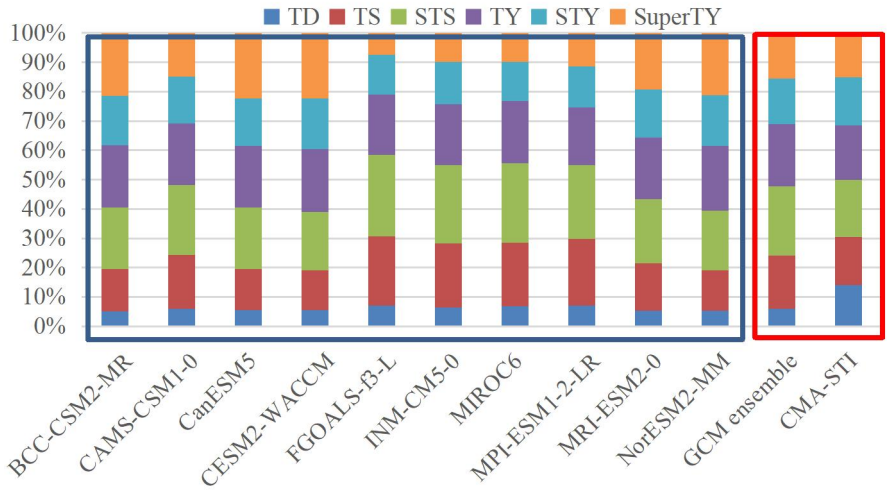


Fig. 4. Proportion of TC Intensity categories across different GCMs in Historical scenario.

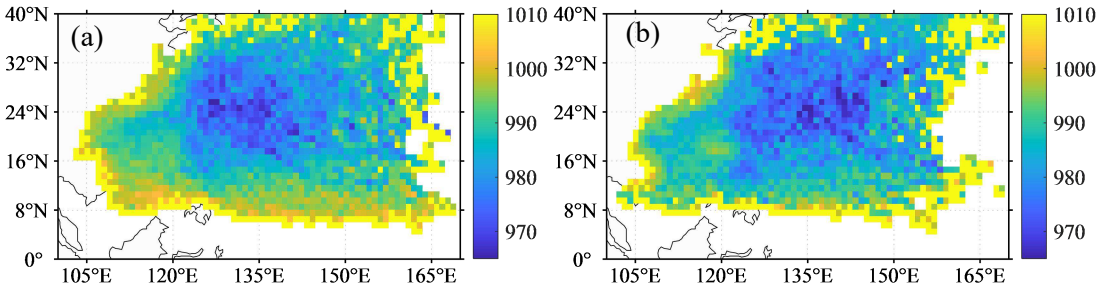


Fig. 5. Spatial distribution of the mean tropical cyclone intensity (represented by mean central pressure, hPa) mapped onto a 1°×1° grid: (a) CMA-STI historical observations and (b) GCM ensemble historical simulations.

To test the spatial performance of the model, the mean intensity field was compared between observations and simulations on a 1°×1° grid, taking the mean central pressure of all TCs passing through each cell. The simulated pattern (Fig. 5b) agrees broadly with the CMA-STI observations (Fig. 5a). Both place the core intensification zone, marked by the lowest mean central pressure, over the open ocean east of Taiwan and the Philippines (about

15°N–25°N, 125°E–145°E), and both reproduce the poleward and coastal decay of intensity. The simulation shows slightly more grid-scale variability than the smoother observations, but the GCM-driven ensemble reproduces the climatological spatial footprint of TC intensity in the WNP adequately.

The simulated LMI climatology was further evaluated against CMA observations in terms of the relative frequency distribution (Fig. 6: blue, CMA observations; gray, individual GCMs; red, GCM ensemble). While the GCM-driven simulations successfully capture the bimodal structure characteristic of rapidly intensifying typhoons, their relative frequency distributions show marked deviations from CMA observations. The GCM ensemble demonstrates improved agreement with the observational data, albeit with a narrower intensity range that underrepresents both extremely weak and strong TCs. This suggests that while pooling the multi-model samples mitigates individual model biases, systematic limitations remain in simulating the full spectrum of TC intensities, particularly for extreme events.

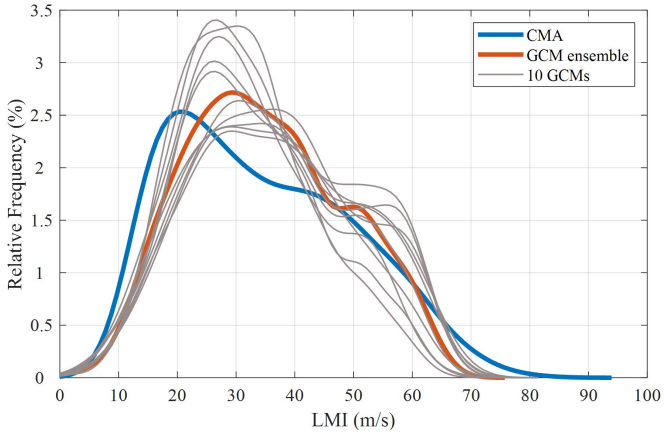


Fig. 6. Relative frequency distribution of simulated TCs' Lifetime Maximum Intensity (LMI) across different GCMs compared with CMA observations. The continuous curves are smoothed using Kernel Density Estimation (KDE). Note: The red 'GCM ensemble' curve denotes the relative frequency distribution estimated from the pooled sample of all simulated TCs generated by the ten individual GCMs (1,000 years per GCM).

The simulated central pressure deficits were then compared with the CMA statistics at the 47 coastal sites (Fig. 8) within the 250-km assessment radius (Vickery et al., 2009; Li and Hong, 2016; Huang et al., 2021), as shown in Fig. 7. Mean deficits differ appreciably between the ten GCMs at each station, mainly because the free-running historical SST fields of the individual models dominate the intensity predictions. The envelope of deficits from all simulated TCs nevertheless contains the CMA observations at most of the 47 stations. The GCM ensemble performs best, with station-level biases within ±4 hPa and a mean absolute error of 1.5 hPa (Fig. 9), outperforming any individual GCM.

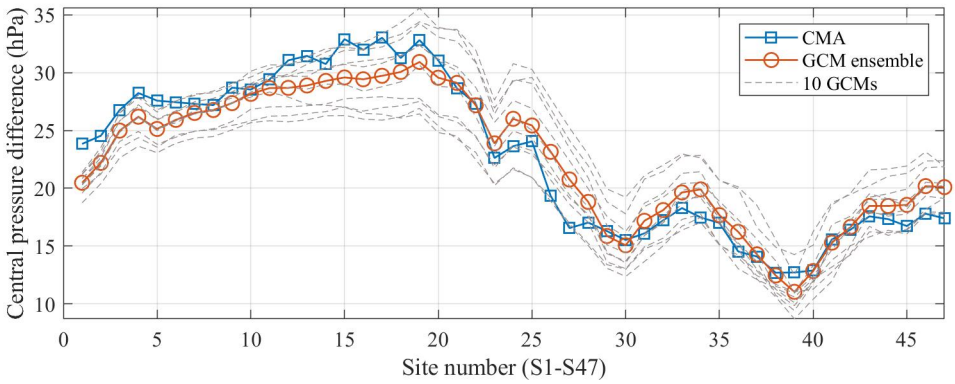
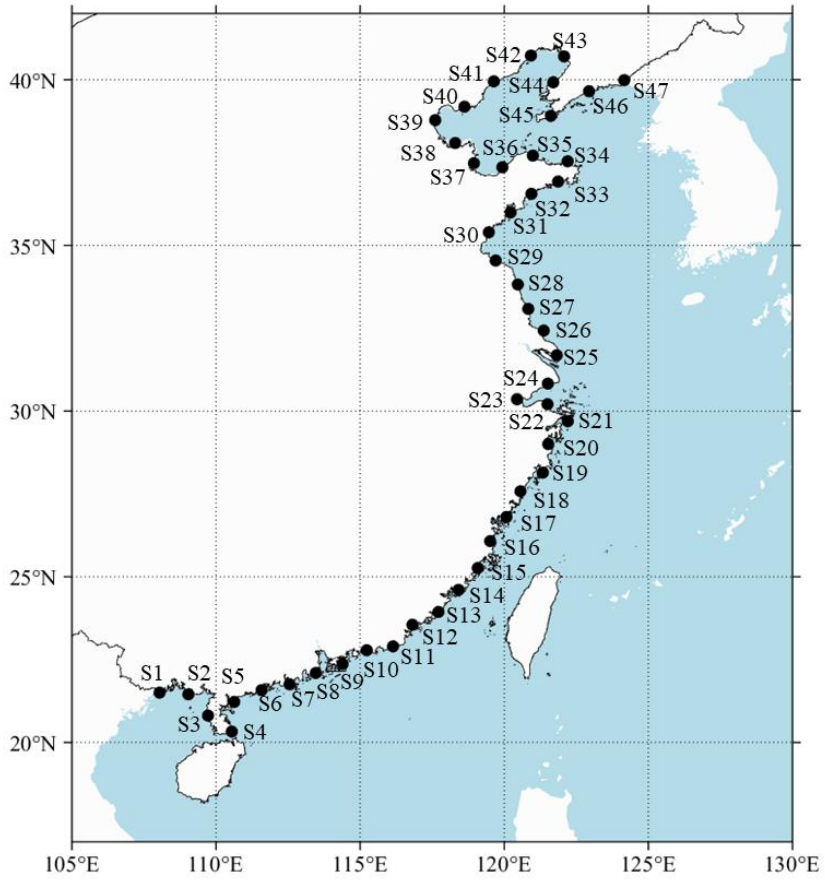
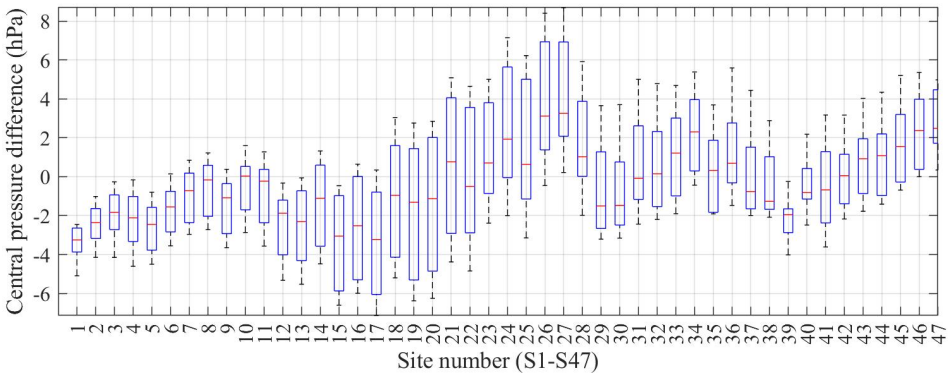


Fig. 7. Central pressure difference of simulated TCs in 47 coastal sites by different GCMs compared with CMA statistical measures.



394

395 Fig. 8. Locations of the 47 selected sites along the coastline of China.



396

397 Fig. 9. Boxplots of the deviation of central pressure difference between the simulated TCs in 47 coastal
398 sites by GCM ensemble with CMA statistical measures.

399 (b) *TC simulation in future climate*

400 Two future periods are examined: the mid-21st century (2019–2055, “Mid”) and the
401 late-21st century (2064–2100, “Late”). The 37-year length follows from the historical baseline

of 1979–2015, which is bounded by the availability of reliable satellite observations and by the end of the CMIP6 historical runs. To keep the sample sizes equal for extreme value analysis, the projections to 2100 are divided into two blocks of the same length; the intervening years 2016–2018 are omitted solely to equalise the windows and do not affect the multi-decadal signals. Monthly mean SST from the WNP under SSP245 and SSP585 was extracted for these periods to drive RFFT.

Changes in the proportions of intensity categories are examined first, using the pooled 10,000-year ensemble (1,000 years per GCM). Each 37-year window is treated as quasi-stationary, and the simulations are driven by the monthly SST field of that window (Section 2.1d). The proportion of TCs at or above typhoon intensity rises in all future climates (Fig. 10), while severe tropical storms and weaker systems become less frequent. Differences between SSP245 and SSP585, and between mid- and late-century, are small. Under SSP245 the proportion at or above typhoon intensity rises by 6.0 percentage points from the Historical period to the mid-century, with super typhoons contributing about 4.4 points, and reaches 60.8% from 52.4% by the late century. More than 60% of WNP TCs are therefore projected to reach at least typhoon intensity by 2100, implying a higher likelihood of severe impacts on coastal cities.

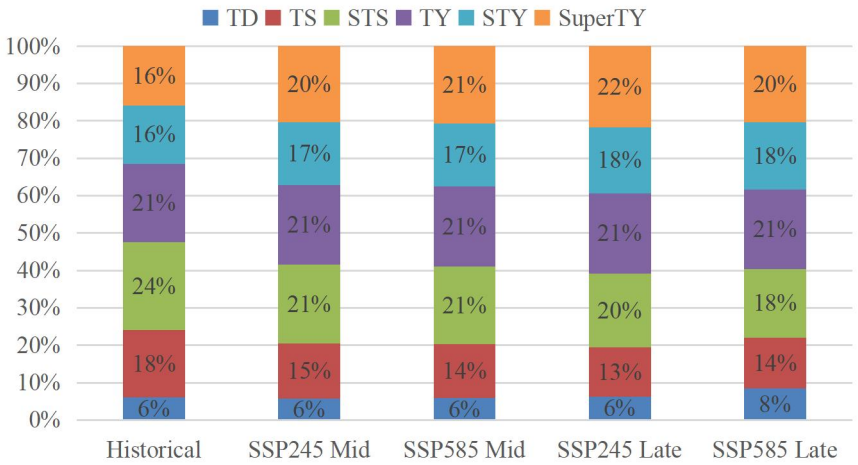


Fig. 10. Proportion of simulated TC intensity categories in different scenarios

Future warming shifts the LMI distribution toward higher intensities (Fig. 11). The main peak of the relative frequency curve moves rightward in future climates, indicating an overall increase in WNP typhoon intensity, and a more pronounced second peak emerges, indicating a higher proportion of rapidly intensifying storms, consistent with the established link between rapid intensification and the bimodal LMI distribution (Lee et al., 2016). The curves differ little between SSP245 and SSP585. Under SSP585, for example, the wind speed at the peak LMI frequency rises from 29.3 m/s in the Historical period to 33.1 m/s (13%) at mid-century and 38.2 m/s (30%) at late century.

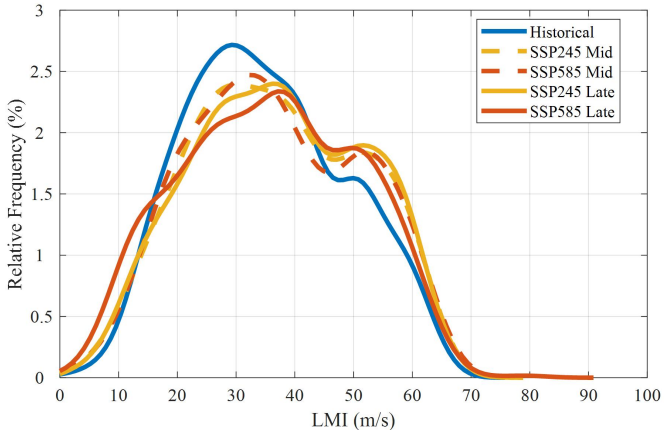


Fig. 11. Relative frequency distribution of simulated TCs' Lifetime Maximum Intensity (LMI) across

the GCM ensemble in different scenarios. The continuous curves are smoothed using Kernel Density Estimation (KDE).

The site-level response along the coast is summarised by the mean central pressure difference within 250 km of the 47 sites (Fig. 12). By the late-21st century SSP585 produces the smallest intensity growth before site S22 and the largest at all later sites; before S22 the largest growth comes from either mid-century SSP585 or late-century SSP245, depending on the site. At the end of the century, however, CanESM5 and CESM2-WACCM give markedly lower intensities at S1–S20 than the other experiments, with similar behaviour in BCC-CSM2-MR and NorESM2-MM. This runs counter to the expected intensification under warmer SST and probably reflects inter-model differences in the projected interdecadal evolution of ocean thermodynamic conditions. The full range of model responses is therefore retained, and the risk assessment uses the pooled ten-GCM ensemble.

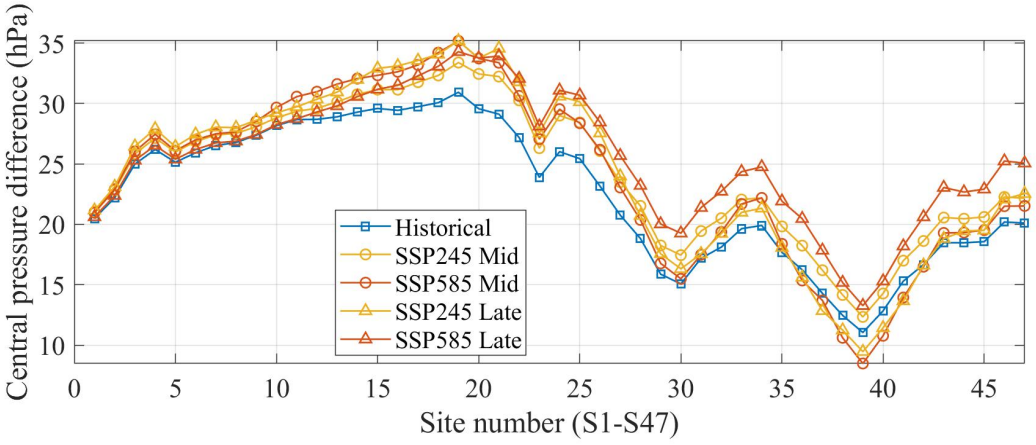


Fig. 12. Central pressure difference of simulated TCs by the GCM ensemble in 47 coastal sites under different scenarios.

3.3 Typhoon wind hazard under changing climate

The preceding sections show that TC intensity will increase under future climate. For

450 engineering purposes the question is how this affects design wind speeds at offshore and
451 coastal sites. This section therefore assesses the typhoon wind hazard for 11 cities along
452 China's southeast coast and then maps the adjacent offshore waters. Following the framework
453 of Section 2, wind fields and extreme speeds are estimated from 10,000-year RFFT ensembles
454 for the Historical climate and for the mid- and late-21st century under SSP245 and SSP585.
455 Each scenario comprises ten 1,000-year simulations, one per GCM, driven by that model's
456 monthly SST field for the corresponding window. Design speeds are estimated separately for
457 each GCM from its own annual-maximum series, and the tabulated values are the mean and
458 standard deviation of the ten estimates; the standard deviation therefore measures inter-model
459 spread, not the uncertainty of the mean. Per-model estimation is preferred to pooling, because
460 the members represent physically distinct climates and pooling would mix heterogeneous
461 populations. Section 3.4 quantifies the adequacy of the 1,000-year length.

462 The annual number of TCs affecting a site is assumed to follow a Poisson distribution. For
463 each GCM, the empirical distribution of its 1,000-year annual-maximum series is used
464 directly, the 50- and 100-year design speeds corresponding to the 98th and 99th percentiles of
465 that series. Any 'return period' statement, and the numerically equivalent Mean Recurrence
466 Interval (MRI) used in codes such as ASCE/SEI 7-22, assumes a stationary climate (Read and
467 Vogel, 2015), an assumption that continuous climate change violates. Each 37-year window is
468 therefore treated as a quasi-stationary climate state, and the reported values are conditional
469 design speeds associated with annual exceedance probabilities of 0.02 and 0.01 under the
470 thermodynamic conditions of that era.

Table 2. Conditional design wind speeds (AEP = 0.02; equivalent to the 50-year return level) of 11 key coastal cities of China under different climate scenarios (units: m/s). Results by HADGEM2-ES (under the CMIP5 RCP8.5 scenario) from Chen et al. (2021) are also listed. Dashes denote unavailable values. Values are the mean and one standard deviation of ten GCM-specific estimates, each obtained from an independent 1,000-year simulation; the standard deviation denotes inter-model spread and is not a confidence interval of the projected change.

City	GB 50009-2012	Historical (1979-2015)	SSP245		SSP585		Chen et al., 2021 (1981-2010)	Chen et al., 2021 (2071-2100)
			Mid	Late	Mid	Late		
Shanghai	29.7	31.9 ± 2.2	33.4 ± 1.7	34.3 ± 1.2	33.9 ± 1.7	34.6 ± 0.7	29.7	31.8
Hangzhou	26.8	29.7 ± 2.0	31.0 ± 1.5	32.0 ± 0.7	31.6 ± 1.2	32.1 ± 0.9	-	-
Ningbo	28.3	34.3 ± 2.2	35.9 ± 1.3	36.6 ± 0.9	36.3 ± 1.2	37.1 ± 1.2	-	-
Wenzhou	31.0	31.8 ± 2.1	32.6 ± 1.1	33.0 ± 0.7	32.7 ± 0.8	33.5 ± 0.8	-	-
Fuzhou	33.5	30.7 ± 1.3	31.4 ± 1.2	31.9 ± 0.4	31.4 ± 1.0	31.7 ± 0.8	30.2	36.5
Xiamen	35.8	34.4 ± 1.2	35.2 ± 0.8	35.6 ± 0.7	35.5 ± 0.6	35.3 ± 0.9	34.0	35.5
Guangzhou	28.3	33.0 ± 1.0	33.7 ± 0.7	33.7 ± 0.7	33.7 ± 0.6	33.1 ± 1.2	-	-
Shenzhen	34.6	36.6 ± 1.0	36.8 ± 0.7	37.0 ± 0.7	36.5 ± 0.7	36.6 ± 1.5	-	-
Hong Kong	37.9	36.0 ± 0.7	36.8 ± 0.6	36.6 ± 0.5	36.6 ± 0.6	36.3 ± 1.3	37.4	38.1
Zhanjiang	35.8	28.2 ± 0.8	28.6 ± 0.6	28.3 ± 0.6	28.3 ± 0.3	28.1 ± 0.7	39.1	40.7
Haikou	34.6	30.6 ± 0.8	31.2 ± 0.6	31.1 ± 0.4	31.3 ± 0.7	30.5 ± 1.1	41.4	37.8

Table 3. Conditional design wind speeds (AEP = 0.01; equivalent to the 100-year return level) of 11 key coastal cities of China under different climate scenarios (units: m/s). Results by HADGEM2-ES (under the CMIP5 RCP8.5 scenario) from Chen et al. (2021) are also listed. Dashes denote unavailable values. Values are the mean and one standard deviation of ten GCM-specific estimates, each obtained from an independent 1,000-year simulation; the standard deviation denotes inter-model spread and is not a confidence interval of the projected change.

City	GB 50009-2012	Historical (1979-2015)	SSP245		SSP585		Chen et al., 2021 (1981-2010)	Chen et al., 2021 (2071-2100)
			Mid	Late	Mid	Late		
Shanghai	31.0	34.3 ± 2.7	35.7 ± 2.1	36.1 ± 1.7	35.7 ± 1.3	37.0 ± 1.3	32.0	34.1
Hangzhou	28.3	32.0 ± 2.2	33.3 ± 1.7	33.4 ± 1.1	33.9 ± 1.8	34.2 ± 1.1	-	-

City	GB 50009-2012	Historical (1979-2015)	SSP245		SSP585		Chen et al., 2021 (1981-2010)	Chen et al., 2021 (2071-2100)
			Mid	Late	Mid	Late		
Ningbo	31.0	36.5 ± 2.2	38.2 ± 1.7	39.0 ± 1.3	38.4 ± 1.5	39.1 ± 1.1	-	-
Wenzhou	33.5	33.8 ± 2.2	35.2 ± 1.7	34.8 ± 1.1	34.4 ± 1.3	35.4 ± 1.1	-	-
Fuzhou	36.9	32.4 ± 1.6	33.3 ± 1.1	33.8 ± 0.7	33.3 ± 0.9	33.5 ± 1.3	34.0	41.7
Xiamen	39.0	36.6 ± 1.0	37.0 ± 0.9	37.6 ± 0.8	36.9 ± 0.6	37.3 ± 0.9	38.2	38.0
Guangzhou	31.0	34.9 ± 1.5	35.4 ± 0.7	35.5 ± 0.6	35.6 ± 1.0	34.8 ± 1.2	-	-
Shenzhen	37.9	38.1 ± 1.0	38.5 ± 0.9	38.4 ± 0.6	38.0 ± 0.8	38.4 ± 1.4	-	-
Hong Kong	39.0	38.0 ± 0.9	38.3 ± 0.7	38.4 ± 0.5	38.3 ± 0.7	38.0 ± 1.7	43.5	46.4
Zhanjiang	39.0	29.4 ± 1.0	30.2 ± 0.8	29.7 ± 0.5	29.7 ± 0.4	29.8 ± 0.7	41.2	46.1
Haikou	37.9	32.3 ± 0.9	32.9 ± 0.8	32.8 ± 0.7	32.6 ± 0.7	32.2 ± 0.9	47.8	40.7

Tables 2 and 3 give the conditional design wind speeds (AEP = 0.02 and 0.01) for 11 key cities from RFFT under historical and future scenarios. Each entry is the mean of the ten GCM-specific estimates and the ±1σ value their standard deviation, i.e. the inter-model spread of the absolute design speed rather than a confidence interval for the projected change. The tables also compare these values with the basic design wind speeds of GB50009-2012 and with the projections of Chen et al. (2021), who used the analogous RCP8.5 scenario of the previous CMIP5 generation.

The definitions of the compared quantities must first be clarified. The simulated speeds are 10-min means at 10 m over open terrain (z_0 = 0.05 m), with no directional, topographic or other engineering adjustment; they are therefore definitionally consistent with the basic design wind speeds of GB50009-2012 and with the hurricane-region basic speeds of ASCE/SEI 7-22, which agree closely with direct hurricane simulations without further adjustment (Vickery et al., 2009). The simulated historical extremes reproduce the observed latitudinal gradient of the hazard (Tables 2 and 3) but range from about 0.8 to 1.2 times the GB50009-2012 values. Three factors contribute to this spread. First, the code values are

statistics from 672 surface stations (Chen et al., 2021), whose record lengths, exposures and terrain corrections differ and whose samples include non-typhoon events. Second, the simulated extremes inherit uncertainty from the CMA best-track intensities, the pressure–wind conversion of the Meng boundary-layer model (Meng et al., 1995) and the simplified drag treatment (Powell et al., 2003). Third, the 250-km assessment radius introduces sampling variability where few storms pass. Deviations of this size are consistent with earlier basin-scale synthetic-TC assessments for China (Chen et al., 2021; Li and Hong, 2016; Huang et al., 2021), and the RFFT framework was validated against the Vickery et al. (2000, 2009) model in earlier work (Huang et al., 2022b).

Two implications follow. First, because the baseline discrepancy (0.8–1.2×) is comparable in magnitude to the projected signal, the absolute simulated speeds should not be used directly as design values. The engineering value of this assessment lies in the relative growth rates, such as the ~7% increase for Shanghai, which act as climate change modification factors applied proportionally to existing engineering baselines. This ratio-based use is defensible because the systematic biases discussed above are approximately state-independent and therefore largely cancel when future and historical estimates from the same model chain are divided; any residual state-dependent bias is acknowledged in Section 3.4. Second, the inter-model spread (±1σ, generally 0.4–2.7 m/s) quantifies substantial epistemic uncertainty, particularly at higher-latitude cities under SSP585, and should inform risk-averse engineering decisions.

Because the same ten GCMs provide both the historical and the future estimate at a given

city, the projected change is examined on the paired differences $\Delta_i = V_{i,future} - V_{i,historical}$, in which each model's climatological bias is largely removed. For SSP585 at the end of the century and AEP = 0.01, the ensemble-mean change is +2.7 m/s at Shanghai, +2.7 m/s at Ningbo and +2.2 m/s at Hangzhou, with 8, 9 and 8 of the ten models agreeing in sign (paired t-test p = 0.020, 0.010 and 0.017). South of Fuzhou the ensemble-mean change is at most +1.1 m/s and cannot be distinguished from zero ($p \geq 0.21$, with 5–7 models positive). The standard deviation of the paired differences (1.6–3.0 m/s) exceeds that of the absolute speeds at most southern cities, so the response itself, not only the climatological bias, differs between models. With ten models the distribution-free sign test requires nine concordant signs to reach $p < 0.05$, which is why the paired t-test is quoted here.

In addition, our thermodynamic-driven projections are more moderate than those of Chen et al. (2021), who reported climate-driven increases exceeding 10% in some East Asian cities (compared with, e.g., 7.9% for Shanghai under SSP585 Late in this study). This discrepancy arises primarily from the differing experimental designs: Chen et al. (2021) incorporated the dynamic evolution of TC tracks and genesis, including a projected poleward shift of TC trajectories, which intrinsically increases landfall frequency at higher latitudes, whereas the present study holds kinematic parameters stationary to isolate the thermodynamic response. Our findings therefore represent the pure thermodynamic amplification of existing typhoon paths, complementing fully coupled dynamic–thermodynamic projections.

Extreme wind speeds increase most strongly at mid- to high-latitude cities (Tables 2 and 3; Fig. 13). Four features stand out. First, mid- to high-latitude cities show substantial and

statistically resolvable increases, whereas low- to mid-latitude cities change within the inter-model spread. Second, growth south of Xiamen stays below 2%, while north of Fujian it exceeds 3%. Third, late-century growth exceeds mid-century growth, and under SSP585 three East China cities (Shanghai, Ningbo and Hangzhou) exceed 6%, peaking at 7.9% in Shanghai. Fourth, late-century SSP585 shows the widest inter-model spread, with no detectable change in Guangzhou, Hong Kong and Haikou ($|\Delta| \leq 0.1$ m/s, $p > 0.8$). Chen et al. (2021) reported a similar pattern, with decreasing 50- and 100-year speeds at five southern cities (Sanya, Haikou, Zhanjiang, Hong Kong and Xiamen) and increasing hazard in northern East Asia. Their mechanism differs, however: the southern decreases follow a projected poleward shift of tracks, whereas with tracks held at the historical baseline the southern changes here are small and lie within the inter-model spread.

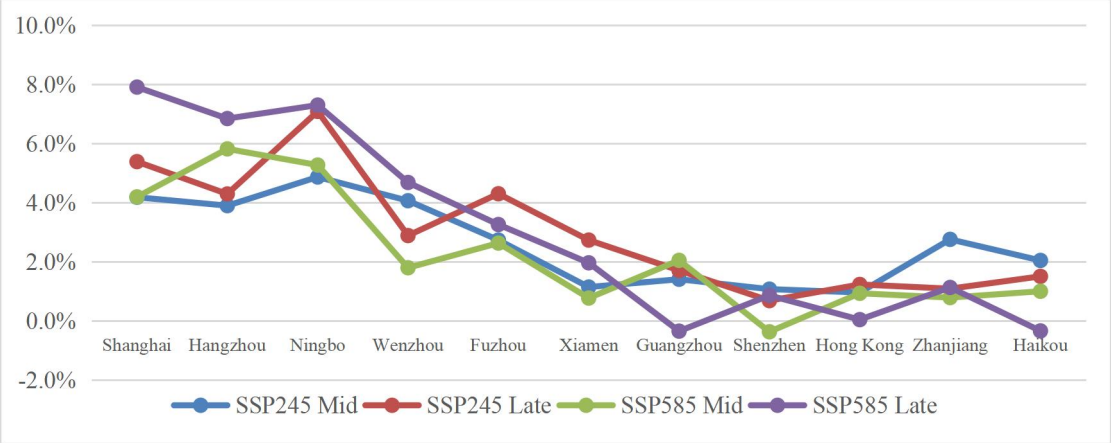
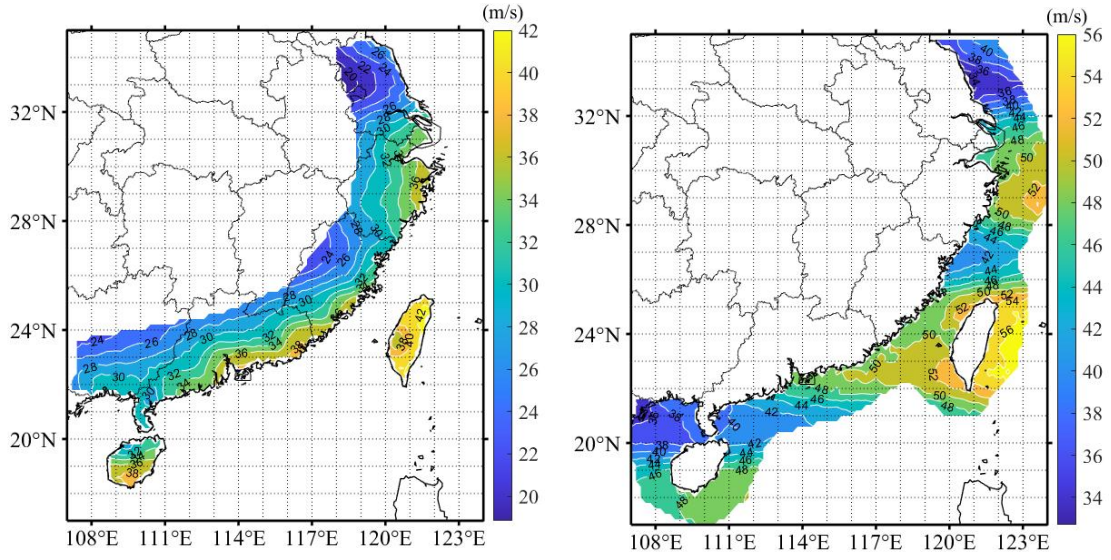


Fig. 13. The growth rates of TC extreme wind speeds under future climates relative to Historical climate estimates for 11 key cities of Southeast China. Growth rates are computed from the ensemble-mean conditional design speeds (AEP = 0.01) as $(V_{future} - V_{historical})/V_{historical}$.

Extreme wind speeds were then computed at every 0.2° grid point over the land and sea

areas of the southeast coast; the resulting 100-year speeds for the Historical climate are shown in Fig. 14. Surface roughness is set to 0.05 m over land, corresponding to Terrain Category B (open terrain) in GB50009-2012 and widely used in earlier regional assessments (Li and Hong, 2016), and to 0.0001 m over water, following the United States Geological Survey definition. A constant sea-surface roughness is a simplification, because the drag coefficient is observed to rise with wind speed and then level off under tropical cyclone conditions (Powell et al., 2003).

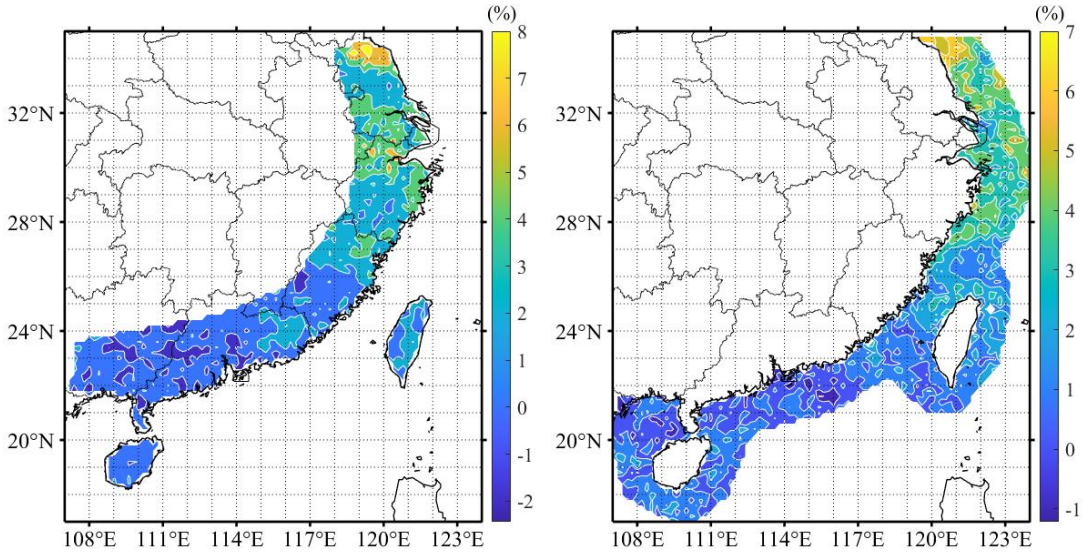
Among coastal land areas, Taiwan faces the highest hazard, with 100-year speeds reaching 40–42 m/s on its Pacific coast. Speeds above 38 m/s also occur from Ningbo to Zhoushan, from Shantou to Zhuhai and in southern Hainan. Offshore (Fig. 14(b)) the maximum lies east of Taiwan, where 100-year speeds exceed 56 m/s. Crossing Taiwan's Central Mountain Range reduces intensity, an effect captured implicitly by the empirical land-decay model (Eq. 5), which is calibrated on historical landfalls; speeds therefore drop to 48–52 m/s between 22°N and 25°N from eastern Guangdong to the Taiwan Strait. Speeds also reach or exceed 48 m/s offshore of eastern Zhejiang and southeastern Hainan. The aerodynamic model represents the transition from sea-surface (z_0 = 0.0001 m) to land-surface roughness (z_0 = 0.05 m) as a step change at the coastline given by the binary land–sea mask. An internal boundary layer treatment would give a smoother and more physical transition but is omitted for computational efficiency in this regional-scale framework, which is a limitation of the present wind-field model.



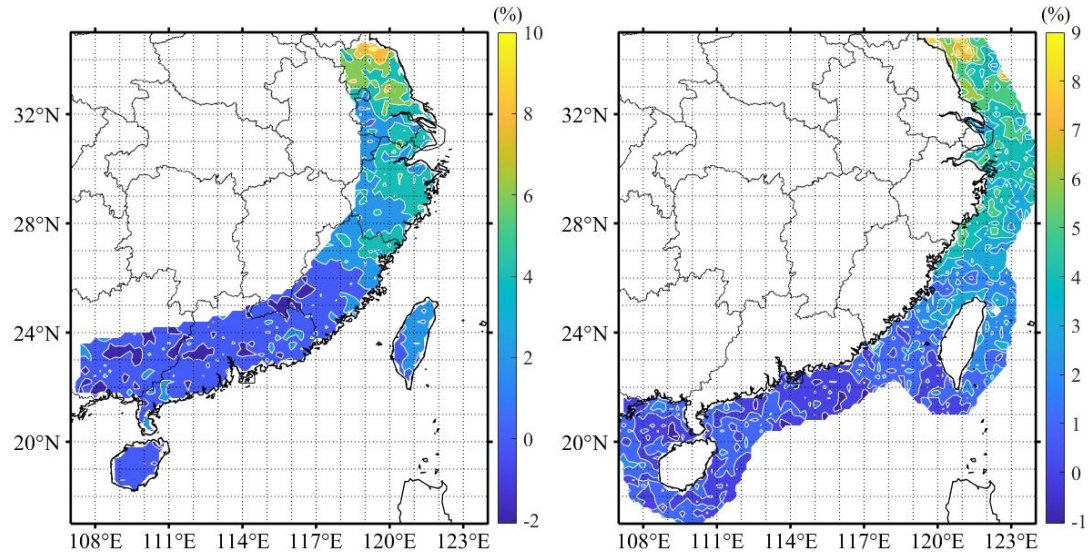
(a)z_0=0.05m (b)z_0=0.0001m

Fig. 14. Typhoon extreme wind speed distributions (0.2° resolution) across the land and sea areas of Southeast China's coast under Historical climate.

By the mid-21st century the growth of extreme wind speed already shows a clear north-high, south-low pattern over both land and sea (Fig. 15a, b for SSP245 and Fig. 15c, d for SSP585). Changes from Hainan to Fujian are minimal, reaching -2% locally, and become progressively larger from Zhejiang to Jiangsu. The largest land increase occurs in northern Jiangsu under SSP585, with a peak growth of 11% and an absolute increase of 2.7 m/s; the largest offshore increase occurs near Jiangsu under the same scenario, at 9.6% and 3.5 m/s. Growth under SSP585 is slightly higher than under SSP245 in every region.



(a)SSP245 z_0=0.05m (b)SSP245 z_0=0.0001m



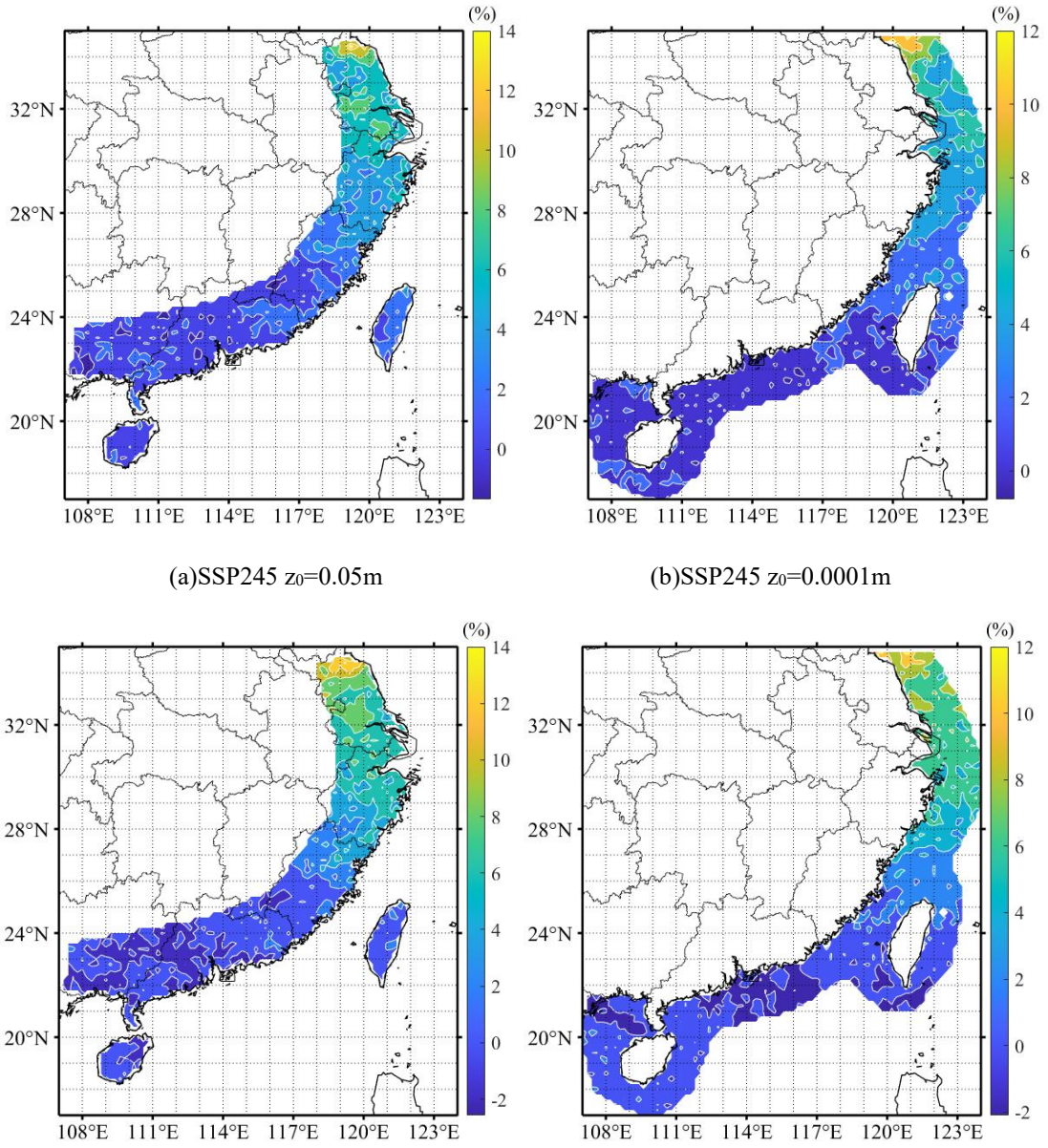
(c)SSP585 z_0=0.05m (d)SSP585 z_0=0.0001m

Fig. 15. The change of typhoon extreme wind speed distributions across the land and sea areas of Southeast China in the mid-21st century relative to the Historical climate.

By the late-21st century the latitudinal amplification is more pronounced (Fig. 16). Growth increases with latitude over both land and sea, and the anomalies again show a positive latitudinal gradient, Jiangsu being the province most affected. South of Zhejiang (near 27°N) SSP245 and SSP585 do not differ significantly, but north of it SSP585 clearly exceeds SSP245, particularly offshore from eastern Zhejiang to northern Jiangsu. The largest growth

602 rates, 15% on land and 14% offshore, both occur near 34°N.

603 The positive latitudinal gradient of the wind speed anomalies follows primarily from the
604 spatial pattern of SST change (Fig. 3), which is strongest in the East China Sea and the Yellow
605 Sea and weakest in the South China Sea, so that the thermodynamic forcing itself is larger at
606 high latitudes. Two further factors act in the same direction. First, the historical design speeds
607 at mid-latitude cities are lower, so the same absolute increase corresponds to a larger relative
608 change. Second, warmer shelf waters allow northward-moving TCs to maintain intensity for
609 longer before the termination criterion is met, which lengthens the exposure of high-latitude
610 sites. The Clausius–Clapeyron relation adds a secondary effect: the fractional increase of
611 saturation vapour pressure per unit warming, $(1/e_s)(de_s/dT) = L/(R_vT^2)$, is larger at lower
612 background temperature, so the same absolute warming raises relative intensity slightly more
613 at high latitudes, even though the absolute increase of e_s is larger in the warm tropics. Within
614 this thermodynamic-only framework the meridional contrast in moist-thermodynamic
615 sensitivity translates directly into the north-high, south-low pattern of hazard amplification, in
616 line with the documented poleward expansion of TC exposure in the WNP (Kossin et al.,
617 2016).



(a)SSP245 z_0=0.05m (b)SSP245 z_0=0.0001m

(c)SSP585 z_0=0.05m (d)SSP585 z_0=0.0001m

Fig. 16. The change of typhoon extreme wind speed distributions across the land and sea areas of Southeast China in the late-21st century relative to the Historical climate.

for coastal and offshore engineering the offshore projections (Figs. 14–16) are of direct value. Over open water, where the observational basis for design conditions is weakest, the framework provides spatially continuous wind fields for an AEP of 0.01 in the historical and each future climate state. Under SSP585, offshore extremes increase by up to 9.6% (mid-century) and 14% (late-century) in the seas offshore of Zhejiang and Jiangsu (the East

China Sea and the southern Yellow Sea), where operating and planned offshore wind farms are concentrated. Because typhoon wind fields are the primary forcing of storm-surge and wave models, the latitudinal amplification documented here implies a systematic, latitude-dependent intensification of surge and wave hazards that should enter the climate-resilient design of offshore wind turbines, platforms and coastal defences.

3.4 Uncertainty and limitations

Two sources of uncertainty affect the projected extremes. The first is climate-model, or epistemic, uncertainty, represented by the inter-model spread (±1σ in Tables 2 and 3). The second is Monte Carlo sampling uncertainty from the finite simulation length. This term was quantified by bootstrapping the 1,000-year annual-maximum series of every city, GCM and scenario (500 resamples each). At AEP = 0.01 the sampling standard deviation of the design speed averages 0.91 m/s (median 0.88, 90th percentile 1.29 m/s), about 2.6% of the design value; at AEP = 0.02 it is 0.68 m/s. A variance decomposition of the paired differences assigns 20–31% of Var(Δ) to sampling at seven of the eleven cities and 39–61% at Hangzhou, Xiamen and Haikou, the remainder being genuine inter-model divergence in the thermodynamic response. Because the historical and future members are independent, sampling noise enters the difference with twice the variance. This is the main reason why the changes are statistically resolvable only at the three northern cities; averaging over ten models reduces the sampling error of the central estimates by about √10, to roughly 0.3 m/s. The 1,000-year length is thus adequate for the ensemble-mean values reported here, but it limits the detectability of change at individual southern cities.

Several limitations of the thermodynamic-only design should be borne in mind. (i) RFFT responds to climate change only through monthly mean SST via the saturation vapour pressure, so projected changes in vertical wind shear, mid-tropospheric humidity and upper-ocean heat content are not represented; the SST-only configuration may therefore under- or over-estimate the thermodynamic intensification. (ii) Genesis locations and rates, track distributions and translation speeds are held at their historical values, whereas evidence for a poleward migration of TC activity (Kossin et al., 2014; Wang and Toumi, 2021) suggests that the higher-latitude increase could be larger. (iii) Each 37-year window is treated as quasi-stationary, so within-window trends are neglected. (iv) The wind-field model uses a constant sea-surface roughness without drag saturation (Powell et al., 2003) and a step change at the coastline. Finally, the ratio-based modification factors assume that model biases are approximately state-independent. These limitations define the scope of the reported factors and set the priorities for further development.

4. Conclusions

This study utilizes monthly mean SST data from ten CMIP6 GCMs, spanning 1979–2100, to analyze the distribution and changes in thermodynamic conditions of the WNP under climate change. Using monthly mean SST from the Historical scenario and the SSP245 and SSP585 scenario simulations, RF-based TC full-track simulations were conducted for historical and future climates to investigate the climate change response of typhoon wind hazards over the China seas and along China's southeast coast. The projections isolate the thermodynamic impact of SST changes on TC intensity, with dynamic factors held at their

historical baselines; the associated uncertainties and limitations are discussed in Section 3.4.

The main findings are as follows:

(1) By the end of the 21st century, the annual mean SST in the WNP is projected to increase by 1.6°C (7.8%) under SSP245 and 3.7°C (18.0%) under SSP585 relative to 2014. High-latitude regions exhibit pronounced warming, with local maximum increases reaching 5°C under SSP585 and 2.5°C under SSP245. Coastal waters adjacent to China warm more strongly than the open ocean at similar latitudes, providing greater potential energy for TC development, particularly along high-latitude coasts.

(2) Compared to the historical period (1979–2015), the proportion of TCs at or above typhoon intensity in the WNP is projected to increase by 6.0 percentage points under SSP245 by the mid-21st century (2019–2055), with super typhoons contributing an increase of 4.4 percentage points. By the late-21st century (2064–2100), over 60% of TCs are projected to reach at least typhoon intensity under SSP245. Overall, typhoon intensity is projected to increase significantly, with a higher proportion of rapidly intensifying typhoons. However, due to systematic biases in the GCM SST fields and in the statistical intensity model, the response of typhoons to climate change varies notably across different climate models.

(3) Extreme wind speed growth along the southeast coast shows a pronounced north-high, south-low pattern in both the mid- and late-21st century. Changes from Hainan to Fujian are minimal, reaching at most -2% locally, but are not distinguishable from zero. North of Fuzhou the increases become statistically resolvable, but only at the three northern cities of Shanghai, Ningbo and Hangzhou (paired t-test $p < 0.05$), and they grow with latitude. Under SSP585

692 northern Jiangsu shows the largest change, with growth of 11% by mid-century and 15% by
693 late century, and offshore trends mirror those on land, reaching 14% by late century. SSP585
694 generally exceeds SSP245, but only modestly. Hazard exposure will therefore increase
695 progressively at higher latitudes, and the offshore amplification over the East China Sea and
696 the southern Yellow Sea should be considered explicitly in climate-resilient design.
697

Acknowledgements

The work described in this paper was partially supported by National Natural Science Foundation of China (Project No. 52478564).

Data availability

The CMIP6 model outputs are publicly available from the Earth System Grid Federation (ESGF) portals (https://esgf-node.llnl.gov/projects/cmip6/). The CMA tropical cyclone best-track dataset is publicly available from the CMA Tropical Cyclone Data Center (https://tcdata.typhoon.org.cn). The synthetic TC ensembles and the derived extreme wind fields generated in this study are available from the corresponding author upon reasonable request.

Declaration of competing interest

The authors declare that they have no known competing financial interests or personal relationships that could have appeared to influence the work reported in this paper.

Declaration of generative AI and AI-assisted technologies in the manuscript preparation process

During the preparation of this work, the author(s) used DeepSeek in order to improve the readability and language of the manuscript. After using this tool/service, the author(s) reviewed and edited the content as needed and take(s) full responsibility for the content of the published article.

References

Arias, P.A., Bellouin, N., Coppola, E., et al., 2021. Technical summary. In: Masson-Delmotte,

V., Zhai, P., Pirani, A., et al. (Eds.), Climate Change 2021: The Physical Science Basis. Contribution of Working Group I to the Sixth Assessment Report of the Intergovernmental Panel on Climate Change. Cambridge University Press, Cambridge, pp. 33–144.

ASCE/SEI 7-22, 2022. Minimum Design Loads and Associated Criteria for Buildings and Other Structures. American Society of Civil Engineers, Reston, VA.

Breiman L, 2001. Random forests. Machine Learning, 45(1): 5-32.

Chen Y, Duan Z, 2018. Impact of ENSO on typhoon wind hazard in the coast of southeast China. Natural Hazards,92(3):1717-1731.

Chen, Y., Duan, Z., Yang, J., Deng, Y., Wu, T., & Ou, J. 2021. Typhoons of western North Pacific basin under warming climate and implications for future wind hazard of East Asia. Journal of Wind Engineering and Industrial Aerodynamics, 208, 104415.

Chu X, Cui W, Zhao L, et al. 2021 Probabilistic flutter analysis of a long-span bridge in typhoon-prone regions considering climate change and structural deterioration. Journal of Wind Engineering and Industrial Aerodynamics,215:104701.

Cui W, Caracoglia L.2016. Exploring hurricane wind speed along US Atlantic coast in warming climate and effects on predictions of structural damage and intervention costs. Engineering Structures,122:209-225.

Cui W, Zhao L, Cao S, et al. 2021. Bayesian optimization of typhoon full track simulation on the Northwestern Pacific segmented by QuadTree decomposition. Journal of Wind Engineering and Industrial Aerodynamics,208:104428.

741 Darling R W R, 1991. Estimating probabilities of hurricane wind speeds using a large-scale
742 empirical model. Journal of Climate, 4(10):1035-1046.
743 Davis C A, 2018. Resolving Tropical Cyclone Intensity in Models. Geophysical Research
744 Letters,45(4):2082-2087.
745 Emanuel K A, Nolan D S, 2004. Tropical cyclone activity and the global climate system. 26th
746 Conf. on Hurricanes and Tropical Meteorology, Miami, FL, Amer. Meteor. Soc.,
747 240–241.
748 Emanuel K, Ravela S, Vivant E, et al., 2006. A statistical deterministic approach to hurricane
749 risk assessment. Bulletin of the American Meteorological Society, 87(3):299-314.
750 Emanuel K A, 2013. Downscaling CMIP5 climate models shows increased tropical cyclone
751 activity over the 21st century. Proceedings of the National Academy of
752 Sciences,110(30):12219-12224.
753 Emanuel K, 2017. Will Global Warming Make Hurricane Forecasting More Difficult?.
754 Bulletin of the American Meteorological Society,98(3):495-501.
755 Eyring V, Bony S, Meehl G A, et al., 2016. Overview of the Coupled Model Intercomparison
756 Project Phase 6 (CMIP6) experimental design and organization. Geoscientific Model
757 Development,9(5):1937-1958.
758 GB50009-2012, 2012. Load code for the design of building structures. China Architecture &
759 Building Press, Beijing (in Chinese).
760 Hausfather Z, Peters G P, 2020. Emissions – the 'business as usual' story is misleading. Nature,
761 577(7792): 618-620.

762 Huang M. F., Wang Q., Li Q., Jing R. Z., et al. , 2021. Typhoon wind hazard estimation by
763 full track simulation with various wind intensity models, Journal of Wind Engineering
764 and Industrial Aerodynamics, 218, 104792.
765 Huang M. F., Wang Q., et al, 2022a. Increasing typhoon impact and economic losses due to
766 anthropogenic warming in Southeast China. Scientific Reports, 12:14048.
767 Huang M. F., Wang Q., Jing R. Z., et al. , 2022b. Tropical cyclone full track simulation in the
768 western North Pacific based on random forests. Journal of Wind Engineering and
769 Industrial Aerodynamics, 228, 105119.
770 Huang M. F., Du H.,Wang Q., et al. , 2024. Extreme wind speed prediction of typhoon for
771 southeast coastal cities and offshore areas of China. Journal of Building Structures,
772 45(05): 104-114 (in Chinese).
773 Hurtt G C, Chini L, Sahajpal R, et al, 2020. Harmonization of global land use change and
774 management for the period 850–2100 (LUH2) for CMIP6. Geoscientific Model
775 Development,13(11):5425-5464.
776 Jing R, Lin N, 2019. Tropical cyclone intensity evolution modeled as a dependent hidden
777 Markov process. Journal of Climate, 32(22): 7837-7855.
778 Knutson T R, Tuleya R E, Kurihara Y, 1998. Simulated Increase of Hurricane Intensities in a
779 CO2-Warmed Climate. Science,279(5353):1018-1021.
780 Knutson T R, Tuleya R E, 2004. Impact of CO2-Induced Warming on Simulated Hurricane
781 Intensity and Precipitation: Sensitivity to the Choice of Climate Model and Convective
782 Parameterization. Journal of Climate,17(18):3477-3495.

783 Knutson T, Camargo S J, Chan J, et al., 2019. Tropical Cyclones and Climate Change
784 Assessment: Part I: Detection and Attribution. Bulletin of the American Meteorological
785 Society,100(10):1987-2007.
786 Knutson, T., Camargo, S. J., Chan, J. L. et al., 2020. Tropical Cyclones and Climate Change
787 Assessment: Part II. Projected Response to Anthropogenic Warming. Bull. Amer.
788 Meteor. Soc. 101, E303–E322.
789 Kossin J P, Emanuel K A, Vecchi G A, 2014. The poleward migration of the location of
790 tropical cyclone maximum intensity. Nature, 509(7500): 349.
791 Kossin J P, Emanuel K A, Camargo S J, 2016. Past and projected changes in western North
792 Pacific tropical cyclone exposure. Journal of Climate, 29(16): 5725-5739.
793 Kossin J P, 2018. A global slowdown of tropical-cyclone translation speed.
794 Nature,558(7708):104-107.
795 Lanzante J R, 2019. Uncertainties in tropical-cyclone translation speed.
796 Nature,570(7759):E6-E15.
797 Lee C Y, Tippett M K, Sobel A H, et al., 2016. Rapid intensification and the bimodal
798 distribution of tropical cyclone intensity. Nature Communications, 7: 10625.
799 Li S H, Hong H P, 2016. Typhoon wind hazard estimation for China using an empirical track
800 model. Natural Hazards, 82(2):1-21.
801 Lu X Q, Yu H, Ying M, et al., 2021. Western North Pacific tropical cyclone database created
802 by the China Meteorological Administration. Advances in Atmospheric Sciences, 38(4):
803 690-699.

804 Marsooli R, Lin N, Emanuel K, et al. , 2019. Climate change exacerbates hurricane flood
805 hazards along US Atlantic and Gulf Coasts in spatially varying patterns. Nature
806 Communications,10(1).
807 Mei, W. & Xie, S., 2016. Intensification of landfalling typhoons over the northwest Pacific
808 since the late 1970s. Nature Geosci, 9, 753–757.
809 Mendelsohn R, Emanuel K, Chonabayashi S, et al., 2012. The impact of climate change on
810 global tropical cyclone damage. Nature Climate Change,2(3):205-209.
811 Meng Y, Matsui M, Hibi K, 1995. An analytical model for simulation of the wind field in a
812 typhoon boundary layer. Journal of Wind Engineering and Industrial Aerodynamics,
813 56(2-3): 291-310.
814 Moon I, Kim S, Chan J C L, 2019. Climate change and tropical cyclone trend.
815 Nature,570(7759):E3-E5.
816 Mudd L, Wang Y, Letchford C, et al. , 2014 Assessing Climate Change Impact on the U.S.
817 East Coast Hurricane Hazard: Temperature, Frequency, and Track. Natural Hazards
818 Review,15(3):4014001.
819 O'Neill B C, Tebaldi C, Van Vuuren D P, et al. , 2016. The Scenario Model Intercomparison
820 Project (ScenarioMIP) for CMIP6. Geoscientific Model Development, 9(9):3461-3482.
821 Park D S R, Ho C H, Kim J H, 2014. Growing threat of intense tropical cyclones to East Asia
822 over the period 1977–2010. Environmental Research Letters, 9(1): 014008.
823 Powell M D, Vickery P J, Reinhold T A, 2003. Reduced drag coefficient for high wind speeds
824 in tropical cyclones. Nature, 422(6929): 279-283.

825 Read L K, Vogel R M, 2015. Reliability, return periods, and risk under nonstationarity. Water
826 Resources Research, 51(8): 6381-6398.
827 Taylor K E, Stouffer R J, Meehl G A, 2012. An Overview of CMIP5 and the Experiment
828 Design. Bulletin of the American Meteorological Society,93(4):485-498.
829 Vickery P J, Skerlj P F, Twisdale L A, 2000. Simulation of hurricane risk in the U.S. using
830 empirical track model. Journal of Structural Engineering, 126(10):1222-1237.
831 Vickery P J, 2005. Simple empirical models for estimating the increase in the central pressure
832 of tropical cyclones after landfall along the coastline of the United States. Journal of
833 Applied Meteorology, 44(12): 1807-1826.
834 Vickery, P.J., Wadhera, D., Twisdale Jr., L.A., Lavelle, F.M., 2009. US hurricane wind speed
835 risk and uncertainty. J. Struct. Eng. 135, 301–320.
836 Wang S, Toumi R, 2021. Recent migration of tropical cyclones toward coasts.
837 Science,371(6528):514.
838 Wu L G, Zhao H K, Wang C, et al., 2022. Understanding of the Effect of Climate Change on
839 Tropical Cyclone Intensity: A Review. Advances in Atmospheric Sciences, 39(2): 205 -
840 221.
841 Xu H, Lin N, Huang M, et al., 2020. Design Tropical Cyclone Wind Speed when Considering
842 Climate Change. Journal of Structural Engineering,146(5):04020063.
843 Ying M, Zhang W, Yu H, et al., 2014. An overview of the China Meteorological
844 Administration tropical cyclone database. Journal of Atmospheric and Oceanic
845 Technology, 31(2): 287-301.

Yu H, Hu C M, Jiang L Y, 2007. Comparison of three tropical cyclone intensity datasets. Acta Meteorologica Sinica, 21(1): 121-127.